remote sensing

MDPI

Article

Measurement of Downwelling Radiance Using a Low-Cost Compact Fourier-Transform Infrared System for Monitoring Atmospheric Conditions

Haklim Choi [1,*] and Jongjin Seo [2,3]

[1] Kyungpook Institute of Oceanography, Kyungpook National University, Daegu 41566, Republic of Korea
[2] Department of Atmospheric and Oceanic Sciences, University of Wisconsin-Madison, Madison, WI 53706, USA; jseo47@wisc.edu
[3] Space Science and Engineering Center, University of Wisconsin-Madison, Madison, WI 53706, USA
* Correspondence: haklim84@knu.ac.kr

Abstract: Temperature and water vapor play crucial roles in the Earth's climate system, and it is important to understand and monitor the variation in the thermodynamic profile within the lower troposphere. Among various observation platforms for understanding the vertical structure of temperature and humidity, ground-based Fourier-transform infrared (FTIR) can provide detailed information about the lower troposphere by complementing the limitations of radiosonde or satellite methods. However, these ground-based systems have limitations in terms of cost, operation, and mobility. Herein, we introduce a cost-effective and easily deployable FTIR observation system designed to enhance monitoring capabilities for atmospheric conditions. The atmospheric downwelling radiance spectrum of sky is measured by applying a real-time radiative calibration using a blackbody. From the observed radiance spectrum, the thermodynamic profile (temperature and the water vapor mixing ratio) of the lower troposphere was retrieved using an algorithm based on the optimal estimation method (OEM). The retrieved vertical structure results in the lower troposphere were similar to the fifth-generation reanalysis database (ERA-5) of the European Center for Medium-range Weather Forecasts (ECMWF) and the National Centers for Environmental Prediction final analysis (NCEP FNL). This provides a potential possibility for monitoring atmospheric conditions by a compact FTIR system.

Keywords: FTIR; hyperspectral; infrared; atmospheric profile; interferogram

Citation: Choi, H.; Seo, J. Measurement of Downwelling Radiance Using a Low-Cost Compact Fourier-Transform Infrared System for Monitoring Atmospheric Conditions. *Remote Sens.* **2024**, *16*, 1136. https://doi.org/10.3390/rs16071136

Academic Editors: Licheng Jiao, Xiangrong Zhang, Yansheng Li, Xu Tang and Lichao Mou

Received: 24 January 2024
Revised: 20 March 2024
Accepted: 22 March 2024
Published: 25 March 2024

1. Introduction

Temperature and water vapor in the atmosphere play crucial roles in the Earth's climatic system. These are critical for the stable energy balance of the Earth, as the atmospheric temperature is a key parameter in the interplay of energy received from the sun and emitted back to space. This balance affects climate change and has direct influences on various meteorological phenomena, which means variations in temperature and water vapor drive the distinct formation of weather patterns and all atmospheric conditions including wind formation and distribution and the intensity of precipitation [1–3].

Particularly, examining the vertical profile of tropospheric temperature and water vapor within the planetary boundary layer (PBL) is crucial for various research applications. These include enhancing operational situational awareness during severe weather events [4], initializing numerical weather prediction (NWP) models [5], facilitating pollution dispersion modeling [6], and conducting research on heat and moisture exchange processes involving the Earth's surface with atmospheric layers [7].

Over the past 60 years, the World Meteorological Organization (WMO) has operated the Global Observing System (GOS), encompassing a comprehensive suite of observations, including surface measurements, aircraft data, ground-based and space-borne remote

sensing, and weather radar observations [8]. This extensive system has been focused on delivering reliable vertical profiles of temperature and water vapor information at a global scale. Furthermore, the Decadal Survey in 2017 highlighted the critical role of thermodynamic profiles within the PBL, emphasizing the need for focused observations as a key area for future investment [9].

Although radiosondes are highly applied as references for their precise and detailed vertical in situ measurements, the limitations in time and space coverage of the radiosonde network are not negligible, due to the costs and labor required for launching these systems. In response to these limitations, advancements in remote sensing technologies have emerged as valuable complements to in situ measurements, fulfilling gaps in the existing operational observing system. Satellite observations, such as those of the Infrared Atmospheric Sounding Interferometer (IASI) onboard the meteorological operational (MetOp) satellites operated by the European organization for the exploitation of meteorological satellite's (EUMETSAT) [10], and the Cross-Track Infrared Sounder (CrIS) onboard the Soumi-National Polar-orbiting Partnership (NPP) jointly operated by the National Oceanic and Atmospheric Administration (NOAA) and National Aeronautics and Space Administration (NASA) [11], offer global-scale coverage and have demonstrated improvements in forecast skills for global Numerical Weather Prediction (NWP) [12]. Despite these advantages, challenges still exist due to the relatively poor horizontal resolution and difficulties in retrievals over iced surfaces, resulting in coarse vertical resolution and accuracy within the planetary layer (PBL) and vertical profiles under cloud cover [13].

Among the various remote sensing observation platforms, ground-based remote sensing instruments, such as the Microwave Radiometer (MWR) [14,15] ground-based Fourier-transform infrared (FTIR), and the Atmospheric Emitted Radiance Interferometer (AERI) [16], offer a highly complementary perspective to space-borne remote sensing. This synergy is derived from their exceptional sensitivity near the Earth's surface and their ability to provide higher vertical and temporal resolution compared to satellite-based remote sensing systems. With an acknowledgement of the importance of mesoscale monitoring and prediction, in 2009, the National Research Council (NRC) stressed the need to develop a global network of ground-based atmospheric profiling systems [17]. In particular, thermodynamic profiles retrieved from the AERI have been used in diverse scientific studies, including those investigating cold fronts and drylines [18], identifying the change in various convective indices in tornadic and non-tornadic storms [4], examining the retrieval method for the cumulus entrainment rate [19], and retrieving aerosol information [20,21]. However, these instruments not only require significant costs to purchase and operate, but also require placement in buildings, ships, or containers, limiting their mobility to specific observation locations. Therefore, an observation system that is more cost-effective and relatively convenient to move to various locations is required to monitor the thermodynamic profile of the lower troposphere.

In this study, we present a compact FTIR system, which offers significant mobility advantages due to its simple installation and stabilization, designed to measure the infrared spectral range for acquiring atmospheric information. Figure 1 shows the overall steps of the proposed observation platform from instrumental setting to the thermodynamic retrieval process, and that flowchart aligns with content flow in this research. In Sections 2 and 3, we introduce the detailed configuration of the instrument, the radiometric calibration method, and the determination of observation characteristics through the signal processing. The retrieval method for thermodynamic profiles from observed sky radiance data is described in Section 4, and Section 5 shows the evaluated results applied to actual observation data.

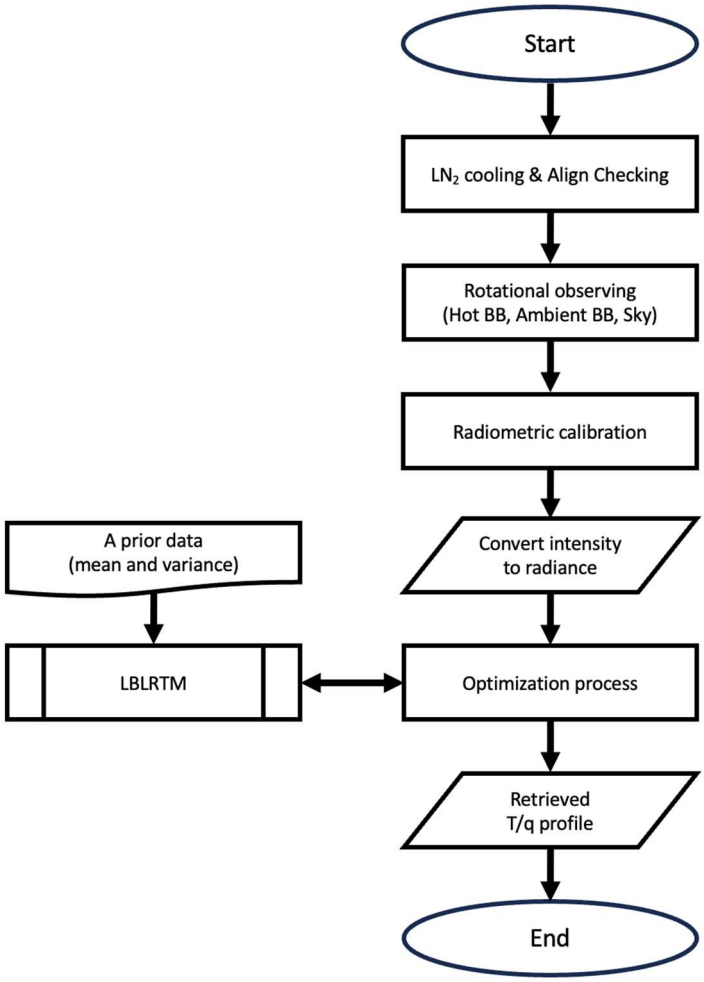

Figure 1. The flowchart from observation to the thermodynamic profile retrieval process.

2. Instrumentation Construction of Instrument Hardware

To measure the atmospheric emitted radiance spectrum and derive atmospheric thermal dynamic profiles, we constructed a compact FTIR observing system using the M4400 spectrometer (Midac Corporation, Irvine, CA, USA). Previously, the MIDAC M4400 spectrometer was primarily used to measure the surface emissivity [22,23] or column gas composition in an open-path FTIR system [24]. Unlike them, we build an additional front-end optical part to the FTIR instrument to acquire atmospheric infrared signals, as shown in Figure 2 (the compact FTIR environment is shown in Figure S1). The entire measurement platform consists of the FTIR instrument part and the front optics part, where the blackbody is located for radiometric calibration of the observation spectrum.

Detailed information on the FTIR and blackbody hardware is described in Table 1. The MIKRON M340 portable blackbody calibration sources (Mikron Instrument Company, Oakland, NJ, USA) for two temperatures (hot and ambient) are located on both sides. The blackbody emissivity is >0.98 within 8–15 μm, covering the atmospheric window. The hot blackbody temperature is fixed at 333 K, while the ambient blackbody temperature varies depending on the surrounding temperature at the time of observation. Blackbody temperatures are easily controlled within 0.1 °C by a self-tuning proportional integral differential (PID) controller from a digital temperature display. A single sky observation consists of a repeating sequence that measures the hot blackbody, sky-view, and ambient blackbody, at one-minute intervals. In the front optics, by adjusting the angle of the switching mirror located in the center of the structure, the incident atmospheric emitted

radiative energy and each blackbody source are transmitted to the FTIR instrument in each sequence.

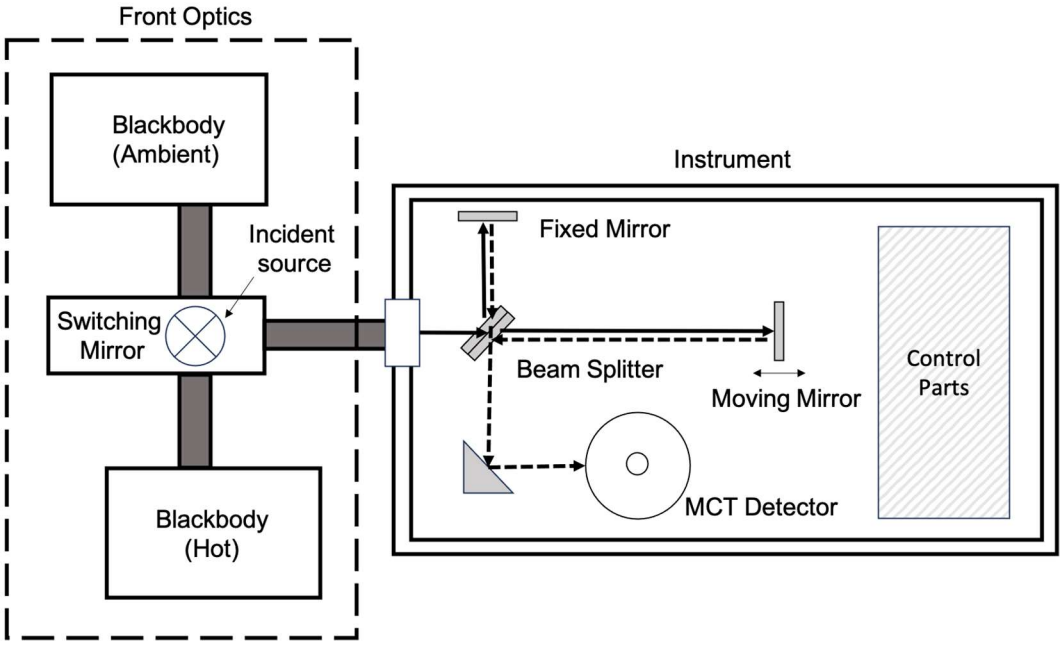

Figure 2. The schematic diagram of the FTIR instrument system. The solid and dashed lines within the instrument represent the path of incoming light before and after being reflected by the mirror.

Table 1. Specification of Instrument and blackbody.

Parameter	Values
FTIR Spectrometer	
Instrument	MIDAC M4400
Type	Michelson interferometer
Mirrors	Gold coated, diamond tuned, permanently aligned
Beam Splitter	KBr
Detector	HgCdTe (MCT; Mercury–Cadmium–Telluride) w/Liquid N_2 cooling
Metrology Laser	HeLe laser
Spectral Range	500 to 4000 cm^{-1}
Spectral Resolution *	1.0 cm^{-1}
Accuracy	>0.01 cm^{-1}
Size	19″ × 11.5″ × 8″ (W × L × H)
Blackbody	
Instrument	MIKRON M340
Temperature Range	−20 °C to 150 °C
Temperature Resolution	0.1 °C
Operating Ambient Temperature	5 °C to 40 °C
Temperature Sensor	Precision Platinum RTD
Stability	0.1 °C per 8 h period
Emitter Diameter	2.0″
Emissivity	0.9756 ± 0.0039 @ 8–15 μm 0.9713 ± 0.0049 @ 3–5 μm
Size	11″ × 11″ × 6.5″ (W × L × H)

* Note, the instrument can be adjusted through software to various resolutions from 0.5 to 32 cm^{-1}. In this study, we used a fixed value of 1.0 cm^{-1}.

MIDAC M4400 FTIR is a Michelson interferometer consisting of a beam splitter, a fixed mirror, a moving mirror, a collimator, and a Mercury–Cadmium–Telluride (MCT) detector. It measures infrared radiance from 500 to 4000 cm^{-1} (2.5–20.0 μm), with an unapodized spectral resolution of 1.0 cm^{-1}. This spectral range of the FTIR platform can cover the various absorption bands of gases in the atmosphere, such as ozone (O_3; 980–1080 cm^{-1}), carbon dioxide (CO_2; 612–618, 624–660, 674–713, and 2223–2260 cm^{-1}), methane (CH_4; 1150–1229 cm^{-1}), and water vapor (H_2O; 538–588, and 1250–1350 cm^{-1}), as well as the atmospheric window (800–1250 cm^{-1}).

The MCT detector is a photon detector, and electrons are directly excited by the absorption radiation. In order to avoid thermal excitation, a cooling system is necessary. Since this FTIR is not equipped with an automated cooling system, liquid nitrogen (LN2) is used to achieve the temperature that acquires a high-sensitivity sensor. When the MCT detector is cooled sufficiently using LN2, which means that the interferogram is stable, the system is ready to observe. Moreover, a desiccant is placed inside, and nitrogen gas is purged due to the high sensitivity of moisture to the major components in the FTIR instrument. To improve the accuracy of the observation spectrum, 32 repeated scans are merged to generate a single spectrum. The observation system is primarily designed for operation under clear sky to avoid interference from rain, and it requires manual operation by human sources, as it is not automated.

3. Signal Processing

3.1. Radiometric Calibration

The atmospheric emitted measured signals by the instrument need to be converted into the known radiometric calibrated radiance unit (i.e., $mWm^{-2}sr^{-1}cm$). As mentioned in Section 2, we performed a two-point radiometric calibration using two well-defined black-bodies (hot and ambient) radiation sources. The single sky-view observation is pairing with measurements of both the hot blackbody and the ambient blackbody at one minute before and after observing sky. Then, the radiometric calibration is performed according to the function described by [25] as follows:

$$N_v = Re\left\{\frac{C_v^s - C_v^A}{C_v^H - C_v^A}\right\}\left(\hat{B}_v^H - \hat{B}_v^A\right) + \hat{B}_v^A \quad (1)$$

$$B(v,\ T) = \frac{2hc^2v^3}{e^{hcv/kT} - 1} \quad (2)$$

where N_v is the calibrated radiance at the wavenumber of v. C_v and $\hat{B}_v$ are the observed spectrum and Plank function radiance at the blackbody temperature (T), respectively. h, c, and k are the Plank constant, the speed of light, and the Boltzmann constant, respectively. The upper labels of A, H, and S denote 'ambient', 'hot', and 'sky', respectively. To obtain the real quantity of the measured spectral data, all values used for radiometric calibration use the real part of the complex [26–28].

3.2. Noise-Equivalent Spectral Radiance

The instrumental responsivity, which represents the conversion factor, can be determined as the inverse of the slope of the radiometric calibration from Equation (1) [28,29].

$$R_v = \frac{C_v^H - C_v^A}{\hat{B}_v^H - \hat{B}_v^A} \quad (3)$$

Because all components of an FTIR spectrometer do not respond perfectly at all wavelengths, the instrument's interferometric response (R_v) varies with changes in wavelength.

The noise-equivalent spectral radiance (NESR), which represents the precision of each measurement, can be determined as the ratio between the standard deviation of the spectrum of repeated measurements and the interferometric responsivity as follows:

$$NESR = \frac{\sqrt{\frac{1}{N}\sum_{i=1}^{N}\left(C_v^{RBB} - \overline{C_v^{RBB}}\right)^2}}{R_v} \quad (4)$$

where C_v^{RBB} represents each individual measured spectrum of all measured spectra as functions of wavenumber at a reference temperature of a blackbody (RBB). N refers to the number of repeated measurements. Figure 3 shows the NESR, calculated from 30 repeated measurements of a blackbody at 300 K, which is the typical atmospheric temperature near the surface (or room condition). The NESR shows a sharp increase in noise driven by influences of CO_2 absorption (around667 cm^{-1}) and water vapor (1400–1700 cm^{-1} and 3000–3500 cm^{-1}) that exist in the interferometric path and the front optics.

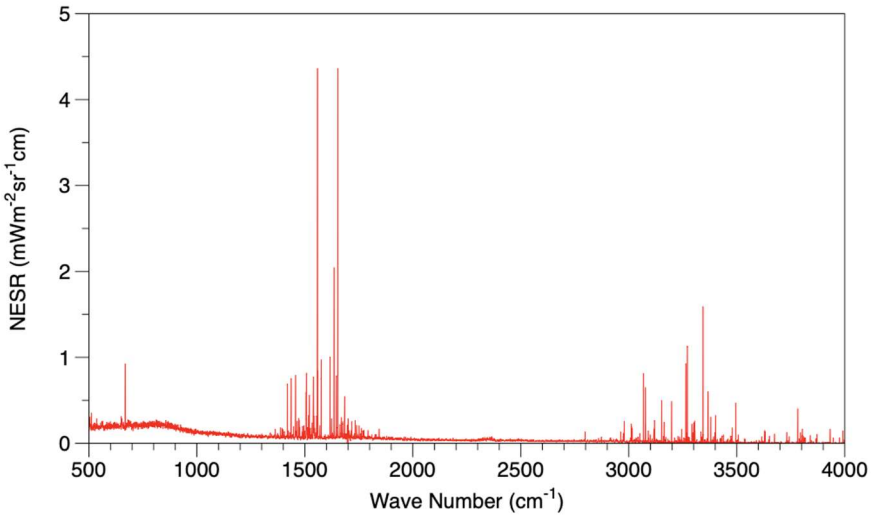

Figure 3. NESR spectra calculated from 30-cycle measurement of blackbody at 300 K from 500 to 4000 cm^{-1}.

4. The Thermodynamic Profile Retrieval Algorithm

4.1. The Line-by-Line Radiative Transfer Model

The monochromatic downwelling radiance, measured at the bottom of the atmosphere (BOA) in the thermal infrared region, is calculated based on contributions from atmospheric layers extending from the ground to the top of the atmosphere. Each atmosphere layer, divided into several sections, is assumed to be a plane-parallel atmosphere with uniform characteristics, such as temperature, pressure, water vapor, and the mixing ratios of various absorbing gases.

$$I_v^{\downarrow}(\mu) = \int_0^{\infty} B(T_z)\frac{d\gamma_v(\mu)}{dz}dz \quad (5)$$

where μ is the cosine of the solar zenith angle. γ_v is monochromatic transmittance. For a specific wavenumber, the optical depth of each layer of the atmosphere can be calculated using the Line-By-Line method by adding the contributions from neighboring absorption lines. The optical depth (τ_v) at a given wavenumber for an atmospheric vertical optical path (Δz) is

$$\tau_v = \Delta z \times \left[\sum_i \left\{\sum_j S_{ji} f\left(v - v_{ji}^0\right)\right\} n_i + \sigma_v^{cont} n_{cont}\right] \quad (6)$$

where S_{ij} denotes the intensity of the line (*j*th) of the species (*i*th). The $f\left(v - v_{ji}^{0}\right)$ term refers to the spectral line-broadening effect centered at v_{ji}^{0}. n_i is the number density of the species (*i*th). $\sigma_v^{cont} n_{cont}$ refers to the contribution of the continuum spectrum.

To simulate the atmospheric transfer process, we adopted the Radiative Transfer Model, LBLDIS, which integrated the Line-By-Line Radiative Transfer Model (LBLRTM) [30,31] to calculate the gas spectral optical depth and Discrete Ordinates Radiative Transfer (DISORT) [32,33] to consider the aerosol effect. In the progress of radiative transfer, the HIgh-resolution Transmission molecular absorption database (HITRAN) 2012 [34], and MlawerTobinCloughKneizysDavies (MT_CKD) [35] are adopted for optical properties of trace gases and water vapor continuum, respectively. The Voight profile was applied to consider for spectral absorption line broadening [36].

4.2. Optimal Estimation Retreival

To retrieve the thermodynamic profile, we apply the physical retrieval algorithm based on the optical estimation method (OEM) [37], which was developed by [21] and has origins in the tropospheric optimal estimation retrieval (TROPoe) algorithm [38] (for the detailed algorithm and performance, refer to [21,38]).

The OEM relies on the Levenberg–Marquardt approach, which provides efficient retrieval of thermodynamic profiles. This optimized method, which uses gradient descent along with the Gauss–Newton methods, iteratively determines the best solution for the non-linear problem. The thermodynamic profiles (iteratively state vector, X^{n+1}) are determined as follows:

$$X^{n+1} = X^{n} + \left[(1+\gamma)S_a^{-1} + K_n^T S_\epsilon^{-1} K_n\right]^{-1}\left[K_n^T S_\epsilon^{-1}(Y - F(X^n)) - S_a^{-1}(X^n - X_a)\right] \quad (7)$$

Here, the a priori of state vector (X_a) and the covariance matrix (S_a) are adopted from the atmospheric composition data of the whole atmosphere community climate model (WACCM) [39]. F(X) represents the radiance spectrum simulated by LBLDIS. K_n is the Jacobian matrix. The standard deviation of the calibrated radiance spectrum is used to calculate the observation error covariance (S_ϵ). The optimized solution minimizes the discrepancy function, named the cost function (c) given by:

$$c = (Y - F(x))^T S_\epsilon^{-1}(Y - F(X)) + (X_a - X)^T S_a^{-1}(X_a - X) \quad (8)$$

The Levenberg Parameter (LP), denoted as γ, acts as a damping factor, Imposing variable weights between the observation and the solution from the preceding iteration step. For high LP values, prior information is given greater weight than observations, while for low LP values, observations are emphasized. The value of LP is determined in each iteration based on the ratio of each step of the cost functions (R), which is calculated as follows:

$$R = (c_n - c_{n+1})/(c_n - c_{n+1,FC}) \quad (9)$$

The calculation of $c_{n+1,FC}$ is based on the assumption of $F(X^{n+1}) = F(X^n) + K_n dX^{n+1}$. The iteration is deemed converged when R falls below 0.25, at which point LP is halved to give more weight to the observations. If R lies between 0.25 and 0.75, LP remains unchanged. However, if R exceeds 0.75, LP is increased tenfold. Convergence at each iteration is determined by:

$$\left(X^n - X^{n+1}\right)^T S^{-1}\left(X^n - X^{n+1}\right) < N \quad (10)$$

N and S are the dimensions of the state vector and the posterior error covariance matrix, respectively. S is determined as:

$$S = \left(\gamma S_a^{-1} + K_n^T S_\epsilon^{-1} K_n\right)^{-1}\left(\gamma^2 S_a^{-1} + K_n^T S_\epsilon^{-1} K_n\right)\left(\gamma S_a^{-1} + K_n^T S_\epsilon^{-1} K_n\right)^{-1} \quad (11)$$

Convergence is declared based on the difference in state vectors between the current and previous iteration steps. This algorithm is applied to discrete continuous spectral bands, as presented in Table 2.

Table 2. Spectral bands utilized for temperature and the water vapor mixing ratio in the retrieval algorithm.

Temperature	Water Vapor Mixing Ratio
612.0–618.0 cm^{-1} 624.0–660.0 cm^{-1} 674.0–713.0 cm^{-1}	1250.0–1350.0 cm^{-1}

5. Results

The experiments were carried out at the Kyungpook National University (Daegu, Republic of Korea; 35.9°N, 128.6°E), using a FTIR observation system for atmospheric observation. Before starting the observation, we sufficiently lowered the temperature of the MCT detector by cooling with LN2. After that, we were able to secure stabilized measurement signals by checking the alignment in real time.

The downwelling atmospheric radiance and the blackbody emitted source (measured by FTIR) are expressed as interference spectra for all wavelengths. Figure 4 shows an example of a short double-sided interferogram measured for an ambient blackbody at 304 K, which shows the commonly named zero path difference (ZPD), i.e., where maximum interference occurs due to the moving mirror in the instrument. The interferogram produced at the ZPD point serves as a reference point for phase correction, since the entire spectral range of the light source produces an ideal interference pattern at this location [40].

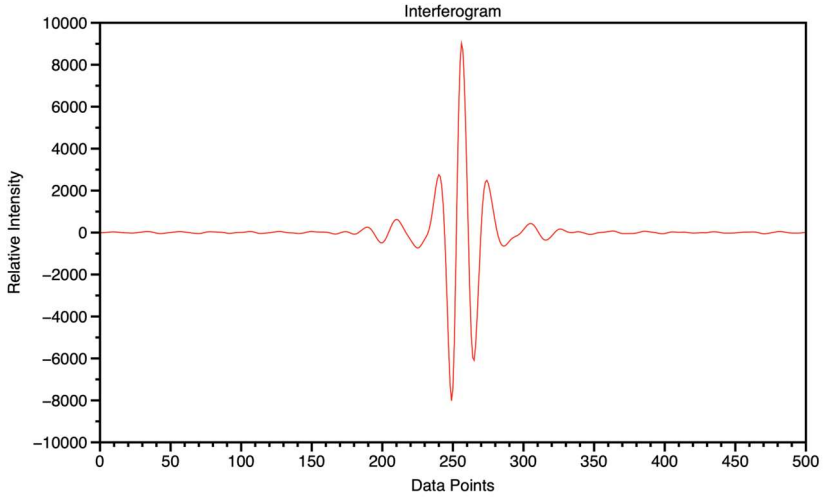

Figure 4. The short, double-sided asymmetric interferogram measure for an ambient blackbody at a temperature of 304 K. The entire interferogram is expressed as a single-sided asymmetric interferogram, as shown in Figure S2.

The interferometric spectrum can be expressed as a function of wavelength in terms of signal intensity using the fast-Fourier transform (FFT). Figure 5 shows the FFT converted measured intensity of the sky view, the hot black body, and the ambient black body from 500 to 4000 cm^{-1} at 0300 UTC on 18 July 2018 (Local Time = UTC + 9 h). The observations have clearly revealed significant features, including the difference in intensity magnitude due to temperature variations between 'hot' and 'ambient' blackbody conditions. Additionally, the atmospheric spectrum fluctuates highly across different wavelengths. Unlike the purged interior of the instrument, the irregular non-smooth spectral shapes at wavelengths of around 667 cm^{-1}, 1400–1700 cm^{-1}, and 3000–3500 cm^{-1} are due to the presence of CO_2 and H_2O in the optical path at the front optics.

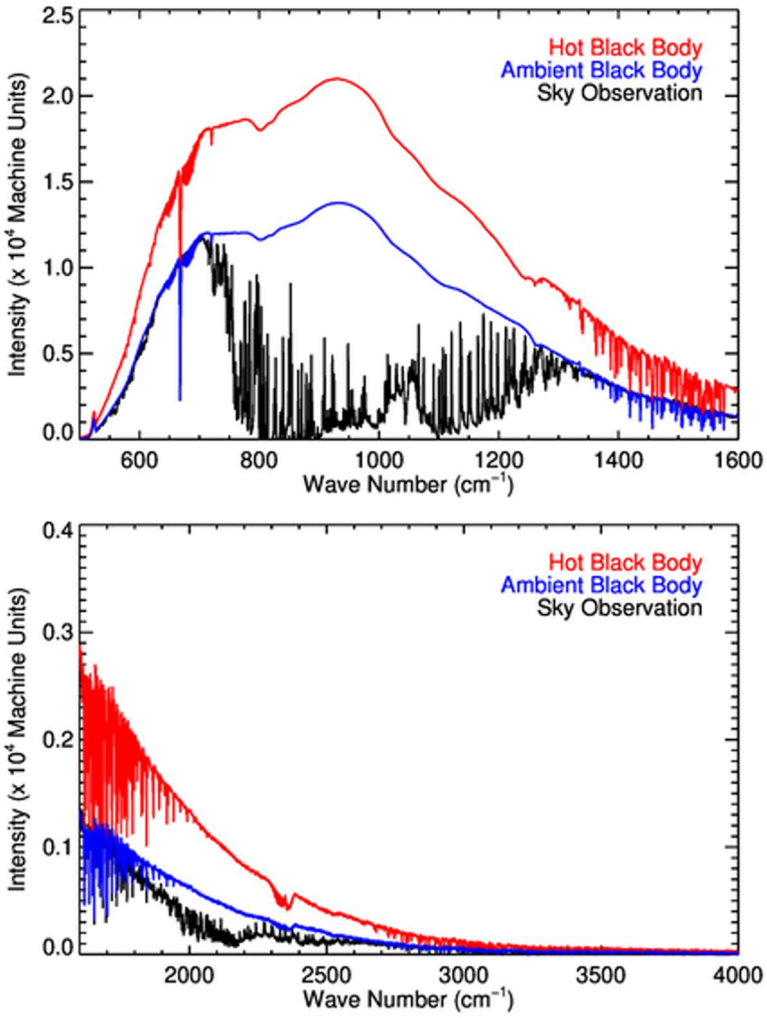

Figure 5. The fast-Fourier transformed observed intensity for sky-view (black) and hot (red) and ambient (blue) blackbody temperatures.

However, the instrument intensity spectrum, expressed in terms of machine unit intensity, does not allow precise delineation of the atmospheric radiation signal targeted for analysis. Therefore, an atmospheric downwelling radiance spectrum could be obtained by conducting a radiometric calibration using Equation 1, as shown in Figure 6. The clear sky condition is insured by the communication, oceanography, and meteorology satellite (COMS) meteorological imager (MI) infrared 1 channel (IR1; 10.8 μm) observations (Figure 7). This 10.8 μm channel measures infrared radiation emitted from the top of cloud and the Earth's surface. Consequently, clouds exhibit a cooler brightness temperature, whereas clear skies display a warmer temperature. The edge curvature of the radiometric calibrated spectrum follows the Planck function of the ambient blackbody temperature between 500 and 4000 cm^{-1}. The observed radiances above 1600 cm^{-1} are very small in magnitude and are not utilized in this study. Generally, the spectrum of atmospheric downwelling radiance in the infrared region is greatly influenced by atmospheric conditions [16,18,20,21]. The spike feature that increases steeply between 650 and 700 cm^{-1} was caused by the emission of CO_2 present in the optical path at the higher temperature, especially due to the CO_2 Q-branch effect. In this way, if the measurement system is not completely purged, the influence of trace gases present inside may be included in the interferogram and radiance spectrum. However, this inevitable influence of CO_2 has little effect because it is not included in the thermodynamic profile retrieval band (Table 2).

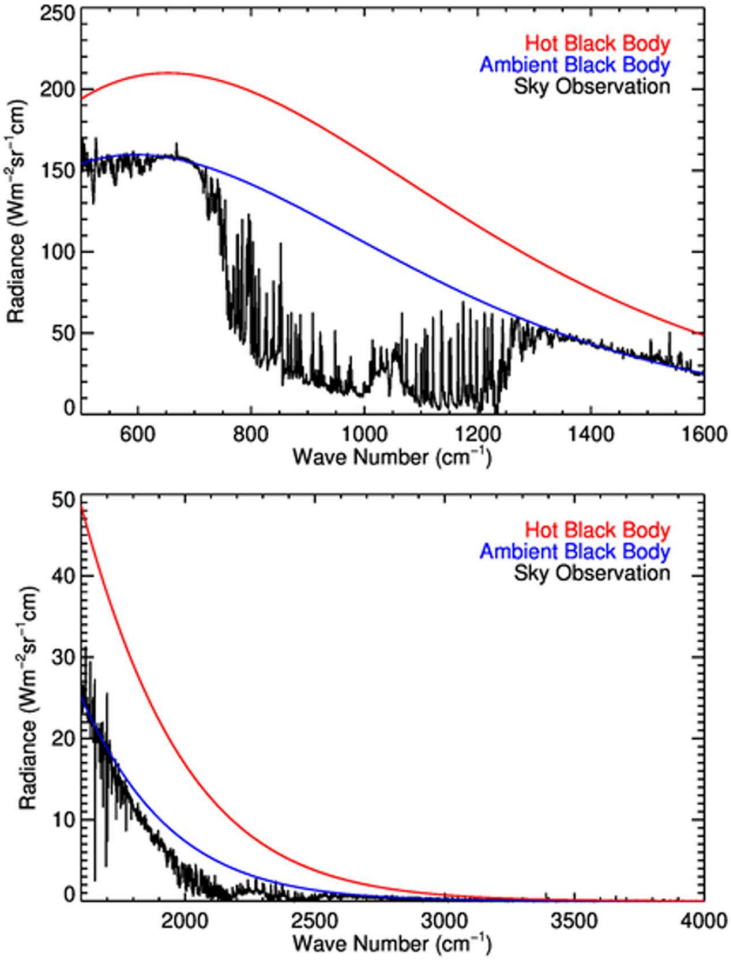

Figure 6. The radiometric calibrated sky downwelling radiance spectrum (black) and Plank function at hot (red) and ambient (blue) blackbody temperatures.

We performed a thermodynamic profile retrieval algorithm using the radiance spectrum generated for clear sky conditions at 0300 UTC on 18 July 2018. Figure 8 shows the changes in the fitting residuals which represent the difference between observations and simulation results for temperature and the water vapor mixing ratio band during the iterative execution of the retrieval algorithm. As spectral fitting was repeated to find an optimal solution, the difference between observed radiance and calculated radiance from the Radiative Transfer Model is decreased, and the Root Mean Square Error (RMSE) of radiance within the fitting spectral region decreases from 3.781 to 0.604 mWm^{-2}sr^{-1}cm.

To investigate the impact of trace gases on the performance of radiance and thermodynamic profile retrieval performance, we generated synthetic radiance using the RTM by adopting thermodynamic profiles from in situ radiosonde data. We performed sensitivity tests for the concentrations of three representative trace gases, CO_2, N_2O and CH_4, for which strong absorption lines exist in the infrared regions. The prior gas concentrations are 410 ppm, 330 ppb, and 1860 ppb, respectively, which are the global average mixing ratios.

Figure 9 shows the change in the radiance spectrum as the concentration of each gas is varied by −1%, +1%, 5%, and 10%. The differences in radiance at ±1% tests are considered negligible. The maximum difference radiance at +10% test is approximately 0.5 radiance unit (RU) for CO_2. This difference is small (within 1 RU) compared to the actual radiance, which ranges from 160 to 165 RU. The range of differences for N_2O and CH_4 is similar to the results of the CO_2 sensitivity test. However, the radiances between 1250 and 1350 cm^{-1} are low at 40–60 RU, so the relative difference is larger than that between 600 and 720 cm^{-1}.

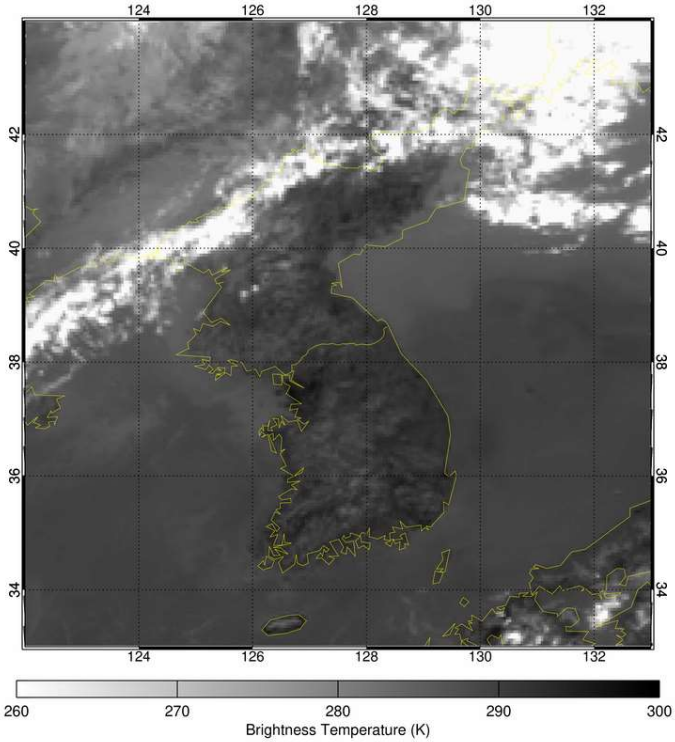

Figure 7. The brightness temperature of communication, oceanography, and meteorology satellite (COMS) meteorological imager (MI) infrared 1 channel (IR1; 10.8 μm) at 0300 UTC on 18 July 2018.

Figure 10 shows the impact of varying the concentration of each trace gas from −1% to +10% thermodynamic profile retrieval. The differences in temperature and water vapor derived from ±1% errors are very small. The maximum difference from 10% concentration uncertainty in temperature is approximately 0.25 K and the water vapor mixing ratio is approximately 0.5 g/kg, respectively. In case of N_2O and CH_4, the differences in temperature, which is approximately 0.9 K, are larger than results from CO_2. However, the maximum differences in water vapor are similar with CO_2 even though the shapes are all distinct between different trace gases. These results indicate that the impact of the concentration of each trace gas on the retrieval of thermodynamic structures is minor. In particular, the effect on temperature below the atmospheric boundary layer (below 1 km) is very small. In actual atmospheric conditions, these trace gases do not vary dramatically, so that the impact from uncertainty of trace gas concentrations can be considered small when prior values are used appropriately.

Figure 11 shows the retrieved thermodynamic profile (temperature and the water vapor mixing ratio) in the lower troposphere below 5 km. To evaluate the thermodynamic profiles obtained from our compact FTIR observations, the retrieved results were compared with those of the fifth-generation reanalysis database (ERA-5) of European Centre for Medium-range Weather Forecasts (ECMWF) [41] and the National Centers for Environmental Prediction Final analysis (NCEP FNL) data [42]. Since both reanalysis meteorological fields are provided at 6 h intervals each day (00, 06, 12, and 18 UTC), the retrieved results were compared accordingly. The ERA-5 data were compared with the 00 UTC analysis, which is 3 h before the actual ground observation time. Meanwhile, the NCEP FNL data were compared with the 03 UTC meteorological field, which is 3 h forecasted from 00 UTC. The derived temperature and water vapor mixing ratio profiles show strong similarities to those from ERA-5 and NCEP FNL, show small differences above 2 km. Notably, the derived surface temperature (33.4 °C) is higher than that of ERA-5 three hours earlier (31.3 °C), and closer to the NCEP FNL (34.3 °C) and the surface temperature from the automated synoptic observing system (ASOS) site of Korea meteorological administration (KMA) (34.1 °C), approximately 4.5 km away from the observation site.

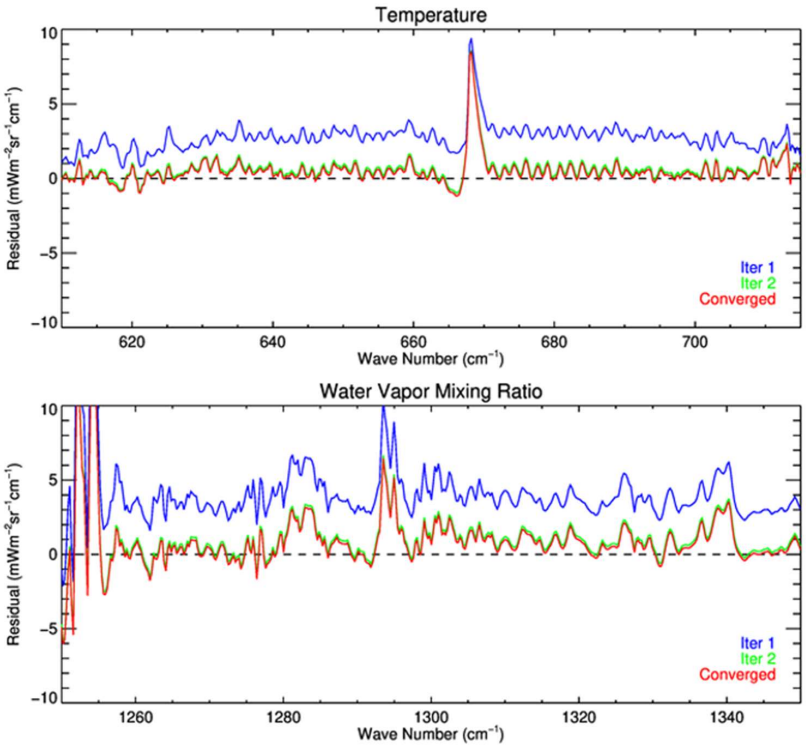

Figure 8. The change in the radiance spectrum residual (observation—simulation) during the iterative retrieval process for temperature and the water vapor mixing ratio. Each color represents each step of iteration.

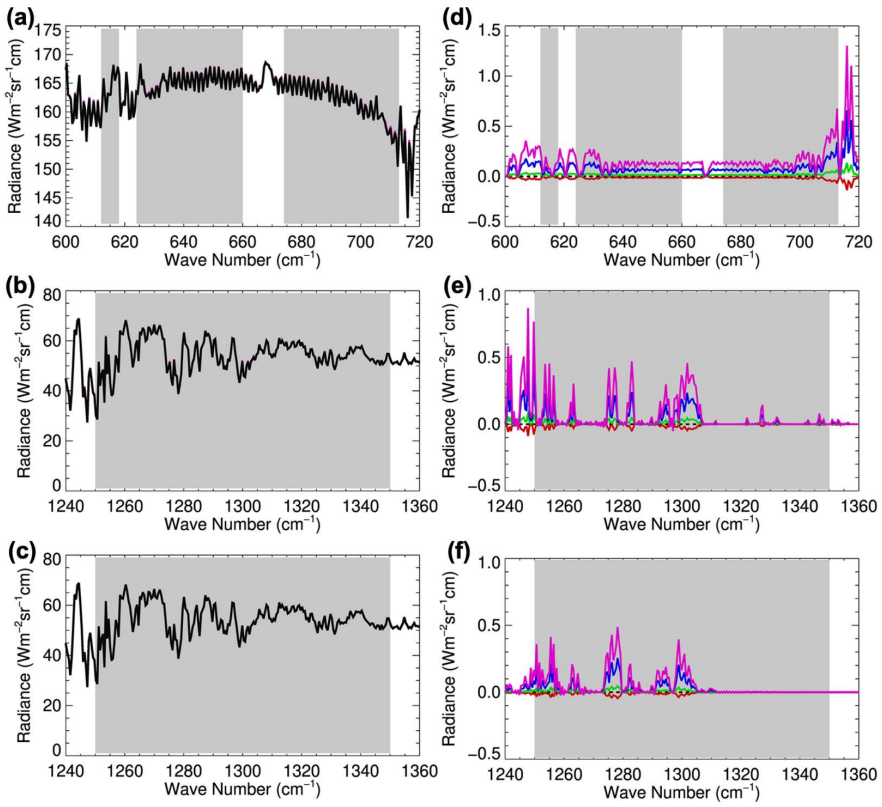

Figure 9. The changes in the radiance spectrum with different concentration of trace gases (**a**,**b**) are for CO_2, (**d**,**e**) are for N_2O, and (**c**,**f**) are for CH_4. Each color represents different concentrations (Red: −1%, green: +1%, blue: +5%, and magenta: +10%).

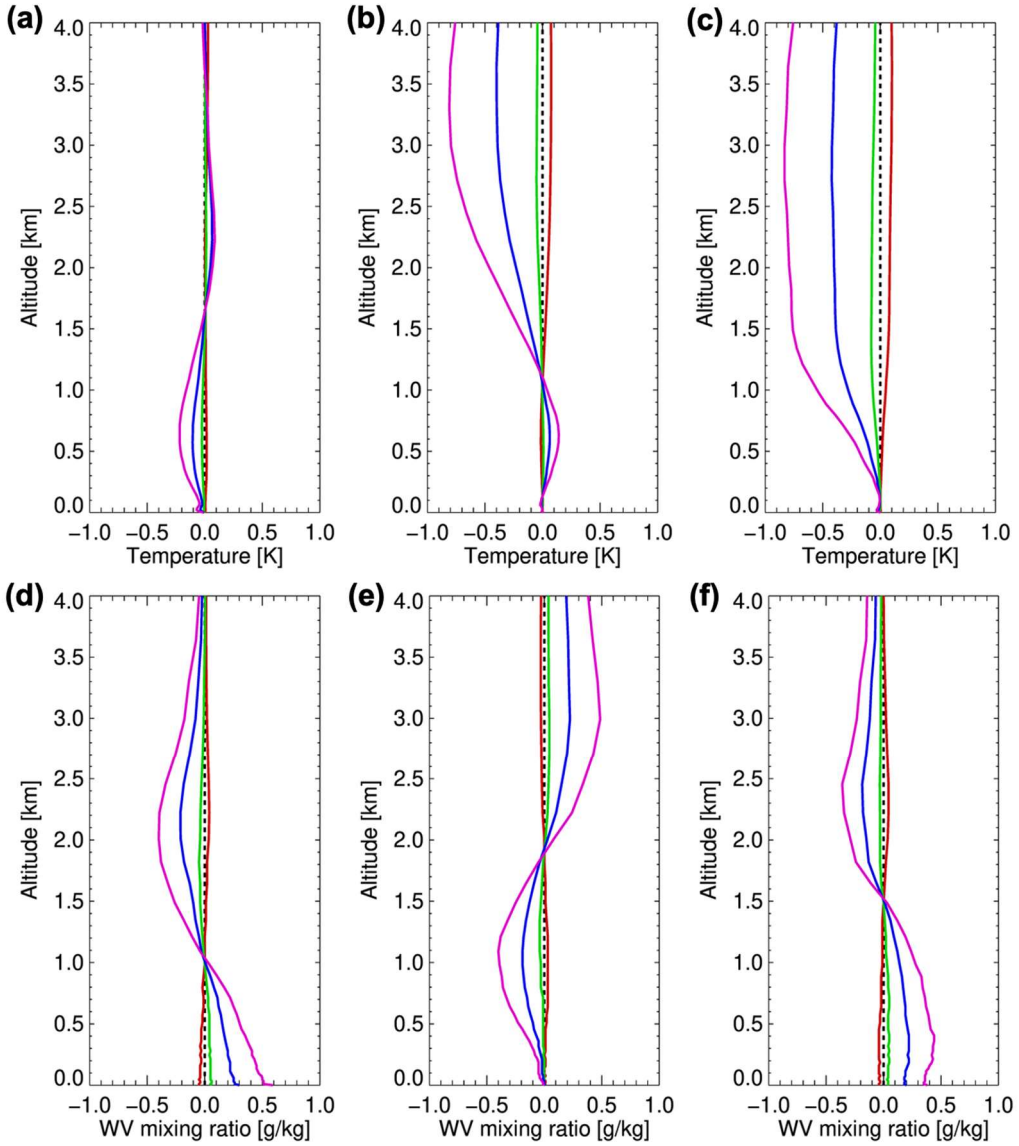

Figure 10. The changes in the retrieved thermodynamic profiles with different concentration of each trace gas, (**a**,**b**) are for CO_2, (**d**,**e**) are for N_2O, and (**c**,**f**) are for CH_4, respectively. Each color represents different concentrations (red: −1%, green: +1%, blue: +5%, and magenta red: −1%, green: +1%, blue: +5%, and magenta: +10%).

This suggests a capture of atmospheric changes due to heating by solar radiation. Particularly, the difference below 2 km with ERA-5 indicates that the downwelling emitted radiance spectrum observed by ground-based FTIR effectively reflects changes in the vertical temperature structure of the lower troposphere. The water vapor mixing ratio profile also shows a very similar feature in vertical distribution and magnitude across the overall altitude. In the lower troposphere, the differences between the three datasets are less than 2 g/kg. These results prove the positive potential for retrieving thermodynamic profiles through a compact ground-based FTIR measurement system and demonstrate the effective performance of the retrieval algorithm.

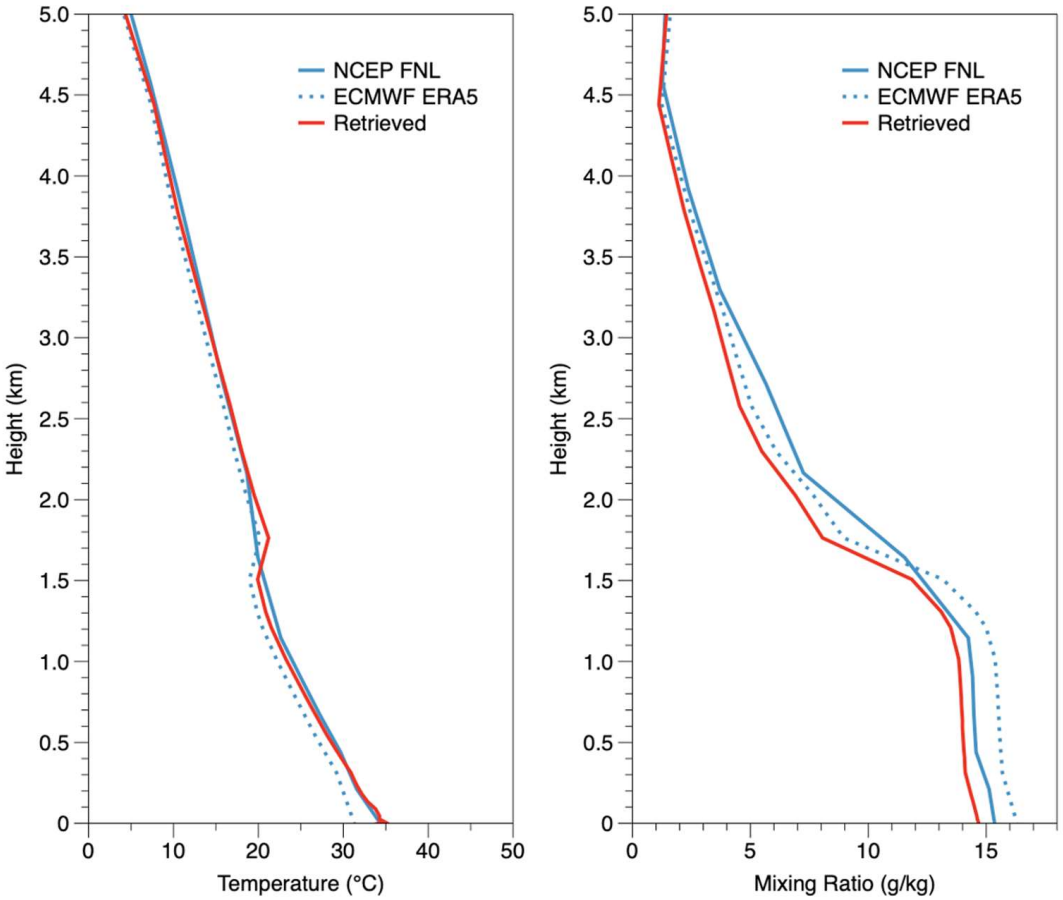

Figure 11. Comparison between the retrieved temperature (**left**) and the water vapor mixing ratio (**right**) with NCEP NFL and ECMWF ERA-5 at 0300 UTC on 18 July 2018.

Since our semi-portable compact FTIR measurement system does not have a rain detection sensor and is manually observed by human labor, the algorithm is designed to operate only under clear sky conditions. Nevertheless, we investigated whether radiance spectrum observations were possible on cloudy days. Figure 12 show the measured radiometric calibrated radiance spectrum for cloudy sky. The observed spectrum shows a significant difference in radiative intensity compared to the simulated spectrum, which assumed clear sky conditions without aerosols and clouds, using NCEP FNL thermodynamic profiles. This difference was predominantly revealed in the spectral range from 700 to 1300 cm^{-1}. This discrepancy is attributed to the influence of clouds. As the clouds become thicker and closer to the surface, the observed radiance spectrum increasingly resembles that of a blackbody. At this time, ASOS recorded a total cloud cover of 30% and the cloud type was Altocumulus (Ac). Additionally, the presence of clouds over the observation site was confirmed in the COMS/MI satellite image. The successful observation of the downward emission radiance spectrum of a cloudy sky suggests that continuous observations, including the effects of clouds, might be feasible in the future.

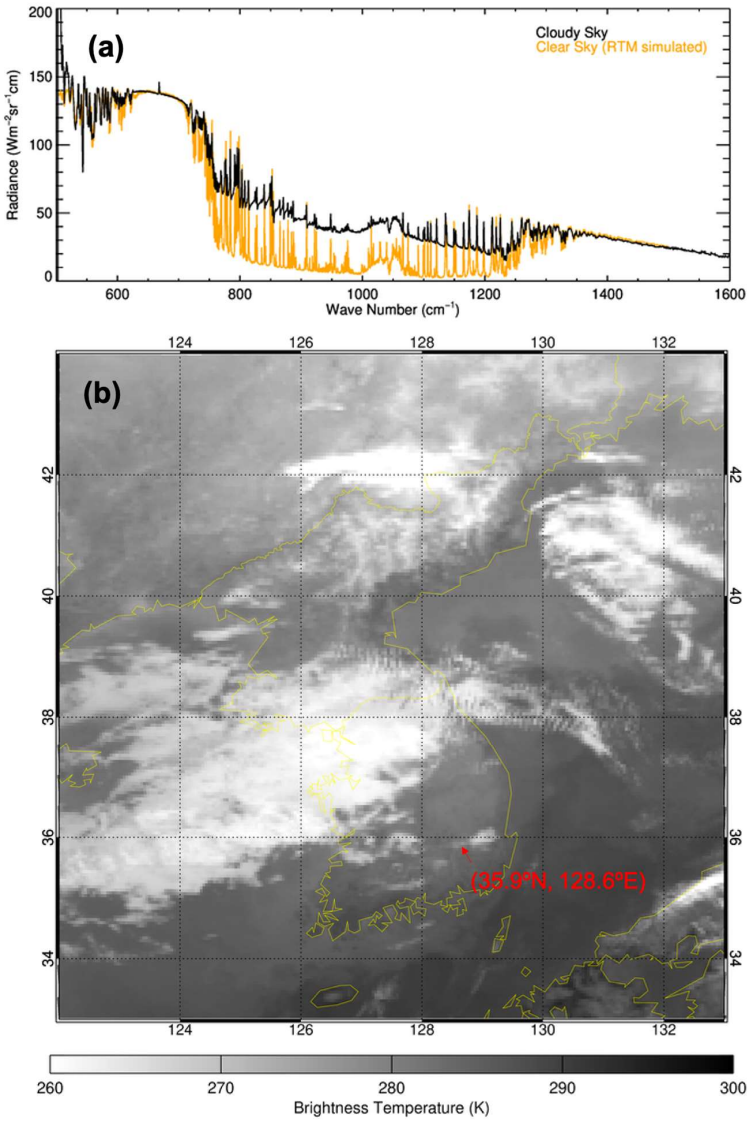

Figure 12. (**a**) The observed radiance spectrum of a cloudy sky at 0300 UTC on 29 November 2018 (black) compared to the radiance spectrum simulated by the RTM, which assumes clear sky conditions (orange). (**b**) The brightness temperature of COMS/MI IR 1 channel at the same time. It can be noticed that clouds exist over the observation site.

6. Discussion

The hyperspectral downwelling emitted radiance is measured using a compact FTIR system configured to real-time radiometric calibration. In this study, the compact FTIR system shows well characterize the downwelling emitted radiance spectrum under both clear and cloudy sky conditions.

However, there are several points that need to be considered when the observation system starts to operate. If the temperature of the MCT detector is not cooled sufficiently or the alignment is not stabilized, the observed interferogram and the radiance spectrum will provide incorrect information. The use of equipment equipped with cryocooling components can minimize the hassle associated with the use of LN2. Additionally, it is necessary to replace periodically the laser source due to aging and desiccants to remove moisture from inside the equipment. After opening the outer casing of the equipment, it should be completely purged using nitrogen gas to minimize the residual effects of CO_2 and H_2O.

The thermodynamic vertical structure of the atmosphere is then estimated using an OEM-based algorithm that uses observed radiance and simulated radiance using the RTM. Consequently, the performance of the retrieval algorithm is sensitive to the intensity of the radiance spectrum as a function of wavenumber, which is simulated by the RTM and takes into account various atmospheric conditions (such as thermodynamic and trace gas profiles) as well as the instrument measurement performance. Because uncertainties from CO_2 line mixing and water vapor continuum absorption used in the RTM are still existing, the accuracy can be improved through continuous efforts about better understanding in radiative transfer equation and optical properties of atmospheric compositions including absorption lines of O_3, as well as the greenhouse gases CO_2 and CH_4. As shown in the O_3 channel spectrum shown in Figure S3, it will be possible to improve the algorithm in the future to simultaneously consider and derive information from these trace gases.

As noted above, the presence of clouds in the atmosphere alters the feature of the radiance spectrum. Unlike the thick clouds shown in Figure 12, which exhibit a significant increase in overall radiance intensity (approaching the blackbody spectrum) compared to clear sky conditions, fractional clouds or cirrus clouds are semi-transparent. This semi-transparency can lead to misidentification, confusing these clouds with conditions of low aerosol optical depth or attributing their effects to atmospheric vertical structures due to water vapor, especially under clear sky conditions. This confusion arises because these clouds have thin optical thickness and emit less energy. Therefore, additional filters or observations are required to distinguish the influence of clouds within the continuous observations. It can be possible to identify and separate signals that are affected by the presence of thin, high altitude cirrus or fractional clouds using cloud information (cloud cover or cloud type) from high-resolution satellites or a ground-based Total Sky Imager (TSI) system.

7. Summary and Conclusions

In this study, we built a compact FTIR system in which the MCT detector is cooled using LN2 and real-time radiometric calibration can be applied using two blackbodies, and the downwelling atmospheric radiance was successfully measured for both clear and cloudy skies. The observed spectrum of the sky reflected the characteristics of the atmosphere and was similar to the spectrum simulated by the RTM, demonstrating the reliable performance of the observation. In addition, the lower troposphere thermodynamic profile obtained using the OEM-based algorithm agreed well with ERA-5 and NCEP FNL data as well as the ASOS surface. Therefore, these results demonstrate the potential of monitoring the thermodynamic profile of the lower troposphere using the compact observation system that we have built. In conclusion, our proposed compact, low-cost FTIR system offers significant cost benefits compared to traditional high-cost instruments. Despite some limitations, such as the need for manual operation and lower accuracy, its portability and real-time observation performance make it a valuable tool for specific applications and field campaigns. This system represents a promising approach for atmospheric observations, especially in scenarios where cost and mobility are critical considerations.

In this study, we used a limited sample of observations to configure an instrument for atmospheric observations and evaluate the applicability of the thermodynamic profile retrieval algorithm in the infrared region. Future work will therefore involve conducting continuous observations and analyzing the variation of the vertical structure of the atmosphere. Through long-term observation, we will be able to check whether systematic drift occurs in the equipment and perform statistical analysis on the accuracy and error characteristics of the results to improve the retrieval algorithm based on this. Identification of the continuous thermal vertical structure of the lower troposphere using compact FTIR can contribute to very short-term forecasting through data assimilation into NWP models in the future.

Supplementary Materials: The following supporting information can be downloaded at: https://www.mdpi.com/article/10.3390/rs16071136/s1, Figure S1: Compact FTIR observation environment and details of equipment configuration. Figure S2: The single-sided asymmetric interferogram measure for an ambient blackbody at a temperature of 304 K. Figure S3: The observed radiance spectrum at 0300 UTC on 18 July, 2018 (black) compared to the radiance spectrum simulated by the RTM (orange) from 1000 to 1100 cm^{-1}. The absorption effect by ozone is clearly revealed in the observed spectrum.

Author Contributions: Conceptualization, H.C.; methodology, H.C. and J.S.; software, H.C. and J.S.; formal analysis, H.C. and J.S.; investigation, J.S. and H.C.; writing—original draft preparation, H.C.; writing—review and editing, H.C. and J.S.; visualization, H.C. and J.S.; supervision, H.C.; project administration, H.C.; funding acquisition, H.C. All authors have read and agreed to the published version of the manuscript.

Funding: This research was supported by the National Research Foundation of Korea (NRF) grant funded by the Korean government (MOE) (no. NRF-2021R1I1A1A01045062).

Data Availability Statement: The data that support the findings of this study are available from the corresponding author upon reasonable request.

Acknowledgments: The authors would like to express their gratitude to the reviewers for their valuable comments and suggestions for improving this manuscript.

Conflicts of Interest: The authors declare no conflicts of interest.

Abbreviations

AERI	Atmospheric Emitted Radiance Interferometer
ARM	Atmospheric Radiation Measurement
ASOS	Automated Synoptic Observing System
BOA	Bottom Of the Atmosphere
COMS	Communication, Oceanography, and Meteorology Satellite
CRIS	CRoss-track Infrared Sounder
DISORT	Discrete Ordinates Radiative Transfer
ECMWF	European Centre for Medium-RangeWeather Forecasts
ERA-5	ECMWF Reanalysis version 5
FFT	Fast Fourier Transform
FTIR	Fourier Transfer Infrared
GOS	Global Observing System
HITRAN	HIgh-Resolution Transmission molecular absorption database
IASI	Infrared Atmospheric Sounding Interferometer
KMA	Korea Meteorological Administration
KNU	Kyungpook National University
LBLRTM	Line-By-Line Radiative Transfer Model
LN2	Liquid nitrogen
LP	Levenberg Parameter
MCT	Mercury–Cadmium–Telluride
METOP	METeorological OPerational
MI	Meteorological Imager
MT_CKD	MlawerTobinCloughKneizysDavies
MWR	Microwave Radiometer
NASA	National Aeronautics and Space Administration
NCEP	National Centers for Environmental Prediction
NESR	Noise-Equivalent Spectral Radiance
NOAA	National Oceanic and Atmospheric Administration
NRC	National Research Council
NPP	National Polar-orbiting Partnership
NWP	Numerical Weather Prediction
OEM	Optimal Estimation Method
PBL	Planetary Boundary Layer

PID	Proportional Integral Differential
RMSE	Root Mean Square Error
RU	Radiance Units
RTM	Radiative Transfer Model
TROPoe	Tropospheric Optimal Estimation Retrieval Algorithm
WACCM	Whole Atmosphere Community Climate Model
WMO	World Meteorological Organization
ZPD	Zero Path Difference

References

1. Trenberth, K.E. Atmospheric moisture residence times and cycling: Implications for rainfall rates and climate change. *Clim. Chang.* **1998**, *39*, 667–694. [CrossRef]
2. Wulfmeyer, V.; Hardesty, R.M.; Turner, D.D.; Behrendt, A.; Cadeddu, M.P.; Di Girolamo, P.; Schlüssel, P.; Van Baelen, J.; Zus, F. A review of the remote sensing of lower tropospheric thermodynamic profiles and its indispensable role for the understanding and the simulation of water and energy cycles. *Rev. Geophys.* **2015**, *53*, 819–895. [CrossRef]
3. Charlesworth, E.; Plöger, F.; Birner, T.; Baikhadzhaev, R.; Abalos, M.; Abraham, N.L.; Akiyoshi, H.; Bekki, S.; Dennison, F.; Jöckel, P. Stratospheric water vapor affecting atmospheric circulation. *Nat. Commun.* **2023**, *14*, 3925. [CrossRef]
4. Wagner, T.J.; Feltz, W.F.; Ackerman, S.A. The temporal evolution of convective indices in storm-producing environments. *Weather Forec.* **2008**, *23*, 786–794. [CrossRef]
5. Dimitrova, R.; Silver, Z.; Zsedrovits, T.; Hocut, C.M.; Leo, L.S.; Di Sabatino, S.; Fernando, H.J.S. Assessment of planetary boundary-layer schemes in the weather research and forecasting mesoscale model using MATERHORN field data. *Boundary-Layer Meteorol.* **2016**, *159*, 589–609. [CrossRef]
6. Miao, Y.; Liu, S. Linkages between aerosol pollution and planetary boundary layer structure in China. *Sci. Total Environ.* **2019**, *650*, 288–296. [CrossRef]
7. Pan, H.-L.; Mahrt, L. Interaction between soil hydrology and boundary-layer development. *Boundary-Layer Meteorol.* **1987**, *38*, 185–202. [CrossRef]
8. World Meteorological Organization (WMO). *Scientific Assessment of Ozone Depletion: 2014*; World Meteorological Organization (WMO): Geneva, Switzerland, 2014; ISBN 9789966076014.
9. Board, S.S.; National Academies of Sciences, Engineering, Medicine. *Thriving on Our Changing Planet: A Decadal Strategy for Earth Observation from Space*; National Academies Press: New York, NY, USA, 2019; ISBN 0309467578.
10. Cayla, F.R. IASI infrared interferometer for operations and research. In *High Spectral Resolution Infrared Remote Sensing for Earth's Weather and Climate Studies*; Springer: Berlin/Heidelberg, Germany, 1993; pp. 9–19.
11. Han, Y.; Revercomb, H.; Cromp, M.; Gu, D.; Johnson, D.; Mooney, D.; Scott, D.; Strow, L.; Bingham, G.; Borg, L. Suomi NPP CrIS measurements, sensor data record algorithm, calibration and validation activities, and record data quality. *J. Geophys. Res. Atmos.* **2013**, *118*, 12734–12748. [CrossRef]
12. Hilton, F.I.; Newman, S.M.; Collard, A.D. Identification of NWP humidity biases using high-peaking water vapour channels from IASI. *Atmos. Sci. Lett.* **2012**, *13*, 73–78. [CrossRef]
13. Huang, H.-L.; Smith, W.L.; Woolf, H.M. Vertical resolution and accuracy of atmospheric infrared sounding spectrometers. *J. Appl. Meteorol. Climatol.* **1992**, *31*, 265–274. [CrossRef]
14. Löhnert, U.; Crewell, S.; Simmer, C. An integrated approach toward retrieving physically consistent profiles of temperature, humidity, and cloud liquid water. *J. Appl. Meteorol. Climatol.* **2004**, *43*, 1295–1307. [CrossRef]
15. Cadeddu, M.P.; Liljegren, J.C.; Turner, D.D. The Atmospheric Radiation Measurement (ARM) program network of microwave radiometers: Instrumentation, data, and retrievals. *Atmos. Meas. Tech. Discuss.* **2013**, *6*, 3723–3763. [CrossRef]
16. Feltz, W.F.; Smith, W.L.; Howell, H.B.; Knuteson, R.O.; Woolf, H.; Revercomb, H.E. Near-continuous profiling of temperature, moisture, and atmospheric stability using the Atmospheric Emitted Radiance Interferometer (AERI). *J. Appl. Meteorol.* **2003**, *42*, 584–597. [CrossRef]
17. Council, N.R. Committee on developing mesoscale meteorological observational capabilities to meet multiple national needs. In *Observing Weather and Climate from the Ground Up: A Nationwide Network of Networks*; The National Academies Press: Washington, DC, USA, 2009.
18. Turner, D.D.; Feltz, W.F.; Ferrare, R.A. Continuous water vapor profiles from operational ground-based active and passive remote sensors. *Bull. Am. Meteorol. Soc.* **2000**, *81*, 1301–1318. [CrossRef]
19. Wagner, T.J.; Turner, D.D.; Berg, L.K.; Krueger, S.K. Ground-based remote retrievals of cumulus entrainment rates. *J. Atmos. Ocean. Technol.* **2013**, *30*, 1460–1471. [CrossRef]
20. Turner, D.D. Ground-based infrared retrievals of optical depth, effective radius, and composition of airborne mineral dust above the Sahel. *J. Geophys. Res. Atmos.* **2008**, *113*. [CrossRef]
21. Seo, J.; Choi, H.; Oh, Y. Potential of AOD retrieval using atmospheric emitted radiance interferometer (AERI). *Remote Sens.* **2022**, *14*, 407. [CrossRef]
22. Lee, Y.-J.; Park, J.-H.; Lee, K.-M. Infrared emissivity of major minerals measured by FT-IR. *Atmosphere* **2015**, *25*, 601–610. [CrossRef]

23. Park, J.; Kim, D.; Kim, H.; Lee, J.; Chung, W. Thermal radiative copper oxide layer for enhancing heat dissipation of metal surface. *Nanomaterials* **2021**, *11*, 2819. [CrossRef] [PubMed]
24. Sellitto, P.; Salerno, G.; La Spina, A.; Caltabiano, T.; Scollo, S.; Boselli, A.; Leto, G.; Zanmar Sanchez, R.; Crumeyrolle, S.; Hanoune, B. Small-scale volcanic aerosols variability, processes and direct radiative impact at Mount Etna during the EPL-RADIO campaigns. *Sci. Rep.* **2020**, *10*, 15224. [CrossRef]
25. Revercomb, H.E.; Buijs, H.; Howell, H.B.; LaPorte, D.D.; Smith, W.L.; Sromovsky, L.A. Radiometric calibration of IR Fourier transform spectrometers: Solution to a problem with the High-Resolution Interferometer Sounder. *Appl. Opt.* **1988**, *27*, 3210–3218. [CrossRef]
26. Bianchini, G.; Palchetti, L. REFIR-PAD level 1 data analysis and performance characterization. *Atmos. Chem. Phys.* **2008**, *8*, 3817–3826. [CrossRef]
27. Knuteson, R.O.; Revercomb, H.E.; Best, F.A.; Ciganovich, N.C.; Dedecker, R.G.; Dirkx, T.P.; Ellington, S.C.; Feltz, W.F.; Garcia, R.K.; Howell, H.B. Atmospheric emitted radiance interferometer. Part I: Instrument design. *J. Atmos. Ocean. Technol.* **2004**, *21*, 1763–1776. [CrossRef]
28. Knuteson, R.O.; Revercomb, H.E.; Best, F.A.; Ciganovich, N.C.; Dedecker, R.G.; Dirkx, T.P.; Ellington, S.C.; Feltz, W.F.; Garcia, R.K.; Howell, H.B. Atmospheric emitted radiance interferometer. Part II: Instrument performance. *J. Atmos. Ocean. Technol.* **2004**, *21*, 1777–1789. [CrossRef]
29. Mathew, G.; Nair, A.; Gundu Rao, T.K.; Pande, K. Laboratory technique for quantitative thermal emissivity measurements of geological samples. *J. Earth Syst. Sci.* **2009**, *118*, 391–404. [CrossRef]
30. Clough, S.A.; Iacono, M.J.; Moncet, J. Line-by-line calculations of atmospheric fluxes and cooling rates: Application to water vapor. *J. Geophys. Res. Atmos.* **1992**, *97*, 15761–15785. [CrossRef]
31. Clough, S.A.; Shephard, M.W.; Mlawer, E.J.; Delamere, J.S.; Iacono, M.J.; Cady-Pereira, K.; Boukabara, S.; Brown, P.D. Atmospheric radiative transfer modeling: A summary of the AER codes. *J. Quant. Spectrosc. Radiat. Transf.* **2005**, *91*, 233–244. [CrossRef]
32. Stamnes, K.; Tsay, S.; Istvan, L. DISORT, a general-purpose Fortran program for discrete-ordinate-method radiative transfer in scattering and emitting layered media: Documentation of methodology. In *DISORT Report v1.1*; Deptartment of Physics and Engineering Physics, Stevens Institute of Technology: Hoboken, NJ, USA, 2000.
33. Stamnes, K.; Tsay, S.-C.; Wiscombe, W.; Jayaweera, K. Numerically stable algorithm for discrete-ordinate-method radiative transfer in multiple scattering and emitting layered media. *Appl. Opt.* **1988**, *27*, 2502–2509. [CrossRef]
34. Rothman, L.S.; Gordon, I.E.; Babikov, Y.; Barbe, A.; Chris Benner, D.; Bernath, P.F.; Birk, M.; Bizzocchi, L.; Boudon, V.; Brown, L.R.; et al. The HITRAN2012 molecular spectroscopic database. *J. Quant. Spectrosc. Radiat. Transf.* **2013**, *130*, 4–50. [CrossRef]
35. Lechevallier, L.; Vasilchenko, S.; Grilli, R.; Mondelain, D.; Romanini, D.; Campargue, A. The water vapour self-continuum absorption in the infrared atmospheric windows: New laser measurements near 3.3 and 2.0 µm. *Atmos. Meas. Tech.* **2018**, *11*, 2159–2171. [CrossRef]
36. Wells, R.J. Rapid approximation to the Voigt/Faddeeva function and its derivatives. *J. Quant. Spectrosc. Radiat. Transf.* **1999**, *62*, 29–48. [CrossRef]
37. Rodgers, C.D. *Inverse Methods for Atmospheric Sounding: Theory and Practice*; World Scientific: Singapore, 2000; Volume 2, ISBN 9814498688.
38. Turner, D.D.; Löhnert, U. Information content and uncertainties in thermodynamic profiles and liquid cloud properties retrieved from the ground-based Atmospheric Emitted Radiance Interferometer (AERI). *J. Appl. Meteorol. Climatol.* **2014**, *53*, 752–771. [CrossRef]
39. Marsh, D.; Mills, M.; Kinnison, D.E.; Lamarque, J.-F. Climate change from 1850 to 2005 simulated in CESM1 (WACCM). *J. Clim.* **2013**, *26*, 7372–7391. [CrossRef]
40. Ben-David, A.; Ifarraguerri, A. Computation of a spectrum from a single-beam Fourier-transform infrared interferogram. *Appl. Opt.* **2002**, *41*, 1181–1189. [CrossRef]
41. Hersbach, H.; Bell, B.; Berrisford, P.; Hirahara, S.; Horányi, A.; Muñoz-Sabater, J.; Nicolas, J.; Peubey, C.; Radu, R.; Schepers, D.; et al. The ERA5 global reanalysis. *Q. J. R. Meteorol. Soc.* **2020**, *146*, 1999–2049. [CrossRef]
42. National Centers for Environmental Prediction/National Weather Service/NOAA/U.S. Department of Commerce. 2015, Updated Daily. NCEP GDAS/FNL 0.25 Degree Global Tropospheric Analyses and Forecast Grids. Research Data Archive at the National Center for Atmospheric Research, Computational and Information Systems Laboratory. Available online: https://rda.ucar.edu/datasets/ds083.3/ (accessed on 23 March 2024).